IEEE Access
Multidisciplinary ⋮ Rapid Review ⋮ Open Access Journal

Received 5 July 2024, accepted 3 August 2024, date of publication 9 August 2024, date of current version 29 August 2024.

Digital Object Identifier 10.1109/ACCESS.2024.3441314

RESEARCH ARTICLE

A Constrained-Based Optimization Method for Real-Time Kinematics Using Magneto-Inertial Signals: Application to Upper Limb Joint Angles Estimation During Prolonged Recordings

MARCO CARUSO[1,2], (Member, IEEE), ELISA DIGO[3], LAURA GASTALDI[2,3], STEFANO PASTORELLI[3,4], AND ANDREA CEREATTI[1,2]

[1]Department of Electronics and Telecommunications, Politecnico di Torino, 10129 Turin, Italy
[2]PolitoBIOMedLab—Biomedical Engineering Lab, Politecnico di Torino, 10129 Turin, Italy
[3]Department of Mechanical and Aerospace Engineering, Politecnico di Torino, 10129 Turin, Italy
[4]Centre for Service Robotics (PIC4SeR), Politecnico di Torino, 10129 Turin, Italy

Corresponding author: Marco Caruso (marco.caruso@polito.it)

This study is part of the project NODES which has received funding from the MUR – M4C2 1.5 of PNRR with grant agreement no. ECS00000036. The content of this publication represents the views of the author only and is his/her sole responsibility; it cannot be considered to reflect the views of the European Commission and/or the MUR. The European Commission and the MUR do not accept any responsibility for use that may be made of the information it contains.

This work involved human subjects or animals in its research. Approval of all ethical and experimental procedures and protocols was granted by the Comitato Etico Territoriale Interaziendale AOU Maggiore della Carità di Novara under Application No. 474/CE 2024.

ABSTRACT This work presents a flexible method for the real-time estimation of human joint angles from magneto-inertial measurement technology. The method aims to enhance the accuracy and consistency of joint angle estimates by incorporating physiological joint limits and task-specific motor characteristics into the optimization process, thanks to a biomechanical model. As an explanatory example, the method was applied to shoulder and elbow joints during a prolonged writing task. The adopted upper limb model was designed following the International Society of Biomechanics guidelines and the Denavit-Hartenberg convention, ensuring anatomical relevance and computational efficiency. By comparing results with stereophotogrammetric tracking outputs, the application of constraints - leveraging a priori knowledge of the workspace boundaries for joint centers - enhanced the accuracy of shoulder and elbow angle estimations and effectively mitigated the impact of sensor orientation drift over extended periods. This method ensured that joint centers trajectories remain within task-specific workspace limits, thus preventing deviations that are not compatible with the expected kinematic behavior. The percentage decrease in the root mean square average errors amounted to about 13% in the time intervals when constraints were active, demonstrating the method's effectiveness in reducing the errors. Computationally time-wise, joint angles were estimated with an update period of about 10 ms, allowing real-time usage. The proposed method can be easily generalized to different biomechanical models and to include information from complementary technologies, making it applicable across various contexts such as clinical assessments, rehabilitation, and ergonomics.

INDEX TERMS Anatomical constraints, human motion tracking, MIMU, IMU, ISB, joint angle estimation, kinematics, magneto-inertial signals, real-time optimization, rehabilitation, sensor fusion, task-specific constraints, upper limb biomechanical model, wearable sensors.

I. INTRODUCTION

The recent diffusion of low-cost wearable magnetic and inertial measurement units (MIMUs) has opened new perspectives for the tracking of human joint kinematics. The most straightforward approach to compute joint kinematics involves estimating the orientation of the MIMUs mounted on adjacent segments in a common global reference frame using a sensor fusion algorithm and then decomposing their relative orientation around the axes of the joints according to

The associate editor coordinating the review of this manuscript and approving it for publication was Angelo Trotta.

a specific rotation sequence [1]. However, the reliability of the joint kinematics is strongly dependent on the quality of the orientation estimates which are jeopardized by stochastic fluctuations and instabilities of the measured angular velocities [2], [3]. The accumulation of these errors during the integration process limits the accuracy of the MIMU orientations to few minutes [4], and, during prolonged recordings the estimated joint angular displacements can be not compatible with the joint physiological limits. Furthermore, inaccuracies in joint orientation estimates can result in incorrect positions of joint centers, determined based on the orientation and length of each segment in a kinematic chain, leading to movements that are not compatible with the specific constraints of the motor tasks being analyzed.

To overcome the above-mentioned issues, particularly critical during prolonged sessions, this study proposed an effective real-time constrained optimization method which allowed to take into account both information about the physiological joint limits [5], [6] (first constraint) and the characteristics associated with the specific motor tasks under analysis (second constraint). Joint angles were obtained by minimizing the difference between MIMU sensor fusion-derived segment orientation and the corresponding orientation based on a biomechanical model. While this approach of minimizing is not unusual for stereophotogrammetric (SP) based methods, it has rarely been used with MIMU signals [5], [6], [7], [8], [9], [10], and, among these few works, none have exploited constraints related to physical task-specific workspace boundaries, focusing solely on physiological joint limits.

The feasibility of the proposed kinematics optimization method was tested through proof-of-concept experiments conducted on one healthy subject performing a prolonged writing task. As an example of application, the method was specifically tailored for the kinematics estimation of the shoulder and elbow joints, considering the orientation of two MIMUs placed on the upper arm and forearm as input. The reference joint kinematics was provided by a marker-based SP system. The focus on the upper limb has been chosen as it is of interest for many applications such as clinics [11], rehabilitation [12], [13], [14], [15], industry [16], [17], sports [18], and ergonomics [19].

The biomechanical model adopted in this work was compliant with the guidelines of the International Society of Biomechanics (ISB) proposed in [20] and designed following the robotic Denavit-Hartenberg (DH) convention. This convention is particularly efficient considering the analogy with a robotic arm [21], [22] and it allows a simple and straightforward description of the kinematic chain which guarantees fast calculations and numerical stability of the obtained angles. Previous literature works have adopted the DH convention to model human upper limbs [23], [24], [25], [26], [27], [28], [29], [30], [31], [32], [33], [34]. However, these works did not consider either the complete upper limb or defined the anatomical axes without following ISB rules, which is central to facilitate clinical interpretability and to compare results with other research findings.

II. MATERIALS AND METHODS

The quantities highlighted in bold refer to vectors. The main symbols introduced in this section are summarized in the Glossary section for reader's convenience.

A. DH UPPER LIMB MODEL

The DH convention defines the pose (i.e., orientation and position) of the j^{th} link with respect to the pose of the $(j-1)^{th}$ link by means of four parameters: two distances (d_j and a_j) and two angles (θ_j and α_j). According to the DH convention [35], each joint is modelled with one degree of freedom allowing a single rotation included in the joint variable ϑ_j. In the proposed model, for each link, d_j, a_j, and α_j are constant and defined based on the geometry of connections between consecutive joint axes only, while θ_j is time-varying, including ϑ_j in addition to a constant offset. Once the axes and the parameters are assigned, the DH convention defines the transformation matrix of the j^{th} link with respect to the previous one in a standard formulation.

The proposed kinematic chain was composed of three rigid segments, namely the trunk (TR), the upper arm (UA), and the forearm (FA) and six revolute joints (Figure 1a). The TR was assumed still, and its coordinate system centered in the shoulder. In detail, the shoulder was assumed as spherical joint allowing three rotations: "plane of elevation" (ϑ_1), "elevation" (ϑ_2), and "intra-extra rotation" (ϑ_3). The elbow was modeled as a universal joint allowing the flexion-extension (ϑ_4) and the pronation-supination (ϑ_6). Moreover, a constant subject-specific carrying angle (ϑ_5) was introduced to model the physiological abduction of FA with respect to UA [23], [36].

The fixed trunk coordinate system was defined by axes (x_0, y_0, z_0) and centered in $\boldsymbol{p}_{TR}$, i.e., the shoulder joint center. $\boldsymbol{p}_{TR}$ was estimated by subtracting, in the vertical direction, from the acromion position the 17% of the distance between the left and right acromion [37], [38] (l AC and rAC), which can be easily identified by palpation.

The UA coordinate system was defined by axes (x_3, y_3, z_3) and centered in $\boldsymbol{p}_{UA}$ (elbow joint center) assumed as the middle point between the lateral and medial epicondyles (LE and ME, Figure 1b), which can be easily identified by palpation. The length of UA (l_{UA}) was the distance between $\boldsymbol{p}_{TR}$ and $\boldsymbol{p}_{UA}$.

The FA coordinate system was defined by axes (x_6, y_6, z_6) and centered in $\boldsymbol{p}_{FA}$ (wrist joint center), coincident with the ulnar styloid process, as suggested by ISB guidelines [20]. It is worth noting that several works considered the wrist joint center as the middle point between the ulnar and radial styloid processes (US and RS, respectively), which diverges from the ISB guidelines. The US and RS can be easily identified by palpation and their distance is $2h$. It follows that the δ rotation

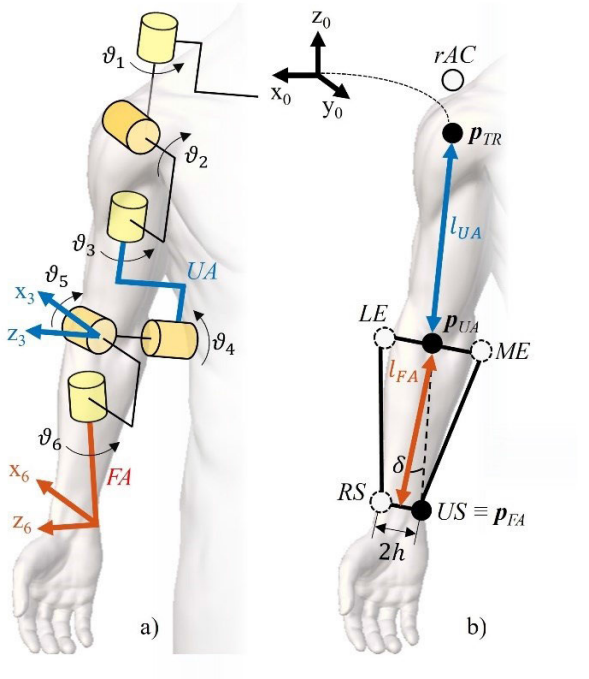

FIGURE 1. a) The DH model of the human upper limb in agreement with the guidelines of ISB. Black segments have null length, whereas blue and red colors are associated to UA and FA, respectively; b) TR, UA, and FA origins are reported with black dots; relevant anatomical landmarks (AC, LE, ME, RS, and US) are reported with white dots; geometrical lengths of UA and FA are reported in blue and red double arrows, respectively.

TABLE 1. The DH parameters and the physiological joint limits.

θ_j	d_j	a_j	α_j	$lower\ limit_j$	$upper\ limit_j$
ϑ_1	0	0	$\pi/2$	$-2\pi/3$	$2\pi/3$
ϑ_2	0	0	$-\pi/2$	0	$11\pi/12$
$\vartheta_3 - \pi/2$	$-l_{UA}$	0	$-\pi/2$	$-2\pi/3$	$2\pi/3$
$\vartheta_4 - \pi/2$	0	0	$-\pi/2$	0	$5\pi/6$
$\vartheta_5 - (\pi/2 + \delta)$	0	0	$-\pi/2$	ϑ_5	ϑ_5
$\vartheta_6 - \pi/2$	$-\frac{l_{FA}}{\cos(\delta)}$	0	$-\pi/2$	0	π

Shoulder: ϑ_1 = plane of elevation, ϑ_2 = elevation, ϑ_3 = intra-extra rotation. Elbow: ϑ_4 = flexion-extension, ϑ_5 = carrying angle (constant value), ϑ_6 = prono-supination. All the angles are expressed in radians.

required to properly center the FA axes in US was obtained by hypothesizing the FA as a planar trapezium (Figure 1b).

$$\delta = tan^{-1}\left(\frac{h}{l_{FA}}\right) \tag{1}$$

The DH parameters were evaluated as reported in Table 1. The last two columns refer to the physiological lower and upper limits for each rotation [39].

For simplicity a_3, a_4, and d_4 were set equal to zero even though, as shown by previous cadaveric studies and as highlighted by Cutti et al. [23], their values are small.

Given a joint configuration $\boldsymbol{\vartheta} = [\vartheta_1, \vartheta_2, \vartheta_3, \vartheta_4, \vartheta_5, \vartheta_6]$ and by applying the DH forward kinematics equations, it was possible to obtain the pose of the UA and FA with respect to the trunk coordinate system. In particular, the 3×3 matrices representing the orientations of the UA and FA are indicated with ${}^0R_{UA}(\boldsymbol{\vartheta})$ and ${}^0R_{FA}(\boldsymbol{\vartheta})$, while the 3×1 position vectors of the elbow and wrist joint centers with ${}^0\boldsymbol{p}_{UA}(\boldsymbol{\vartheta})$ and ${}^0\boldsymbol{p}_{FA}(\boldsymbol{\vartheta})$, respectively. For notation simplicity, the "0" superscript will be hereafter omitted.

B. KINEMATICS OPTIMIZATION METHOD

For sake of clarity, the optimization method is presented with reference to the specific problem of the upper limb kinematics during a writing exercise. However, a similar methodology can be generalized and applied to different kinematic models and motor tasks. The hat superscript ^ refers to quantities obtained from the sensor fusion algorithm starting from MIMU raw signals.

The optimization relied on the minimization between the modelled UA and FA orientations, $R_{UA}(\boldsymbol{\vartheta})$ and $R_{FA}(\boldsymbol{\vartheta})$, with the corresponding MIMU-based sensor fusion orientations ($\hat{R}_{UA}$ and $\hat{R}_{FA}$, calculated as detailed in paragraph D). Their relative orientations were computed as follows:

$$\begin{aligned} R_{\Delta UA} &= R_{UA}(\boldsymbol{\vartheta})\left(\hat{R}_{UA}\right)^T \\ R_{\Delta FA} &= R_{FA}(\boldsymbol{\vartheta})\left(\hat{R}_{FA}\right)^T \end{aligned} \tag{2}$$

Then, $R_{\Delta UA}$ and $R_{\Delta FA}$ were mathematically converted into the corresponding axis-angle representations. Their angular values, γ_{UA} and γ_{FA}, were extracted as follows [35]:

$$\begin{aligned} \gamma_{UA} &= \cos^{-1}\left(\frac{tr\left(R_{\Delta_{UA}}\right) - 1}{2}\right) \\ \gamma_{FA} &= \cos^{-1}\left(\frac{tr\left(R_{\Delta_{FA}}\right) - 1}{2}\right) \end{aligned} \tag{3}$$

where the tr function in (3) represents the trace of the matrix. The nonlinear multivariable objective function f_{obj} to be minimized was finally defined as:

$$f_{obj}(\boldsymbol{\vartheta}) = \gamma_{UA}^2 + \gamma_{FA}^2 \tag{4}$$

It is worth pointing out that the joint configuration $\boldsymbol{\vartheta}$ which aligns $R_{UA}(\boldsymbol{\vartheta})$ and $R_{FA}(\boldsymbol{\vartheta})$ with their counterparts $\hat{R}_{UA}$ and $\hat{R}_{FA}$, respectively, also results in $R_{\Delta UA}$ and $R_{\Delta FA}$ being equivalent to the identity matrices (2). In this case, γ_{UA} and γ_{FA} would be zero (3) as well as $f_{obj}(\boldsymbol{\vartheta})$. To avoid joint angles to exceed their physiological range and to force the elbow and wrist centers to lie within their physical workspace boundaries, the minimization of $f_{obj}(\boldsymbol{\vartheta})$ was constrained to $\boldsymbol{g}_1(\boldsymbol{\vartheta})$ and $\boldsymbol{g}_2(\boldsymbol{\vartheta})$ functions. Mathematically the problem was formulated as follows:

$$\min f_{obj}(\boldsymbol{\vartheta}) \text{ subject to } \begin{cases} \boldsymbol{g}_1(\boldsymbol{\vartheta}) \\ \boldsymbol{g}_2(\boldsymbol{\vartheta}) \end{cases} \tag{5}$$

The equations for $\boldsymbol{g}_1(\boldsymbol{\vartheta})$ are defined in (6).

$$\boldsymbol{g}_1(\boldsymbol{\vartheta}) = lower\ limit_j \leq \vartheta_j \leq upper\ limit_j \quad \forall j = \{1, 2, 3, 4, 6\} \tag{6}$$

In (6) index $j = 5$ is omitted, since the carrying angle ϑ_5 is a constant value, according to Table 1. In general, the formulation for $\boldsymbol{g}_2$ can include any nonlinear function of $\boldsymbol{\vartheta}$. In this work, the equations for $\boldsymbol{g}_2$ are defined on the elbow and wrist trajectories as in (7)

$$\boldsymbol{g}_2(\boldsymbol{\vartheta}) = \begin{cases} \boldsymbol{p}_{UA}(\boldsymbol{\vartheta}) \in WS_e \\ \boldsymbol{p}_{FA}(\boldsymbol{\vartheta}) \in WS_w \end{cases} \tag{7}$$

where WS_e and WS_w are the generic sets defining the three-dimensional workspace boundaries in which the elbow and wrist centers must be confined. This problem was solved by defining the Lagrangian function $\mathcal{L}(\boldsymbol{\vartheta}, \boldsymbol{\lambda}, \boldsymbol{\sigma})$:

$$\mathcal{L}(\boldsymbol{\vartheta}, \boldsymbol{\lambda}, \boldsymbol{\sigma}) = f_{obj}(\boldsymbol{\vartheta}) - \sum_{n=1}^{N} \lambda_n g_{1n}(\boldsymbol{\vartheta}) - \sum_{m=1}^{M} \sigma_m g_{2m}(\boldsymbol{\vartheta}) \tag{8}$$

and then finding the optimal values of $\boldsymbol{\vartheta}, \boldsymbol{\lambda}, \boldsymbol{\sigma}$ which lead to $\nabla\mathcal{L} = 0$. The quantities $\boldsymbol{\lambda}$ and $\boldsymbol{\sigma}$ represent the Lagrangian multipliers applied to $\boldsymbol{g}_1(\boldsymbol{\vartheta})$ and $\boldsymbol{g}_2(\boldsymbol{\vartheta})$, respectively. In general, $\boldsymbol{\lambda}$ and $\boldsymbol{\sigma}$ are vectors with a length depending on the number of inequalities defined (i.e., N and M). Obviously, even if applied, $\boldsymbol{\lambda}$ and/or $\boldsymbol{\sigma}$ are only effective for those time intervals when (6) and/or (7) are not respected, otherwise the optimal $\boldsymbol{\vartheta}$ would be equal the same as if the constraints were not applied. The numerical solution for the optimal $\boldsymbol{\vartheta}, \boldsymbol{\lambda}, \boldsymbol{\sigma}$ values was iteratively found using an optimization solver such as the Sequential Quadratic Programming (SQP), which is suitable for non-linear constrained optimization problems [40].

The implementation method shown in Figure 2 was designed to find the optimal joint configuration at each i^{th} time-step.

For each iteration, given a $\boldsymbol{\vartheta}, \boldsymbol{\lambda}, \boldsymbol{\sigma}$ configuration, the objective function definition requires the computation of $R_{UA}(\boldsymbol{\vartheta})$ and $R_{FA}(\boldsymbol{\vartheta})$. Then equations (2)-(4) were applied to quantify $f_{obj}(\boldsymbol{\vartheta})$. The lower and upper limits required by (6) were defined for each ϑ_j according to Table 1. To implement (7), the $\boldsymbol{p}_{UA}(\boldsymbol{\vartheta})$ and $\boldsymbol{p}_{FA}(\boldsymbol{\vartheta})$ were first computed by applying the DH forward kinematics. The workspace boundaries WS_e and WS_w were assumed as horizontally oriented parallelepipeds. The validity of (7) was established in two sequential steps. Firstly, the point-in-polygon algorithm [41] was applied to the (x, y) coordinates of $\boldsymbol{p}_{UA}(\boldsymbol{\vartheta})$ and $\boldsymbol{p}_{FA}(\boldsymbol{\vartheta})$ enforcing the elbow and wrist positions to lie inside the horizontal projection of E and W, respectively. Subsequently, the z-coordinates of $\boldsymbol{p}_{UA}(\boldsymbol{\vartheta})$ and $\boldsymbol{p}_{FA}(\boldsymbol{\vartheta})$ were limited to the minimum and maximum values of the E and W vertical projections. Finally, the $\mathcal{L}$ was quantified according to (8). The SQP iteratively refined the solution by adopting a sequential approach to update $\boldsymbol{\vartheta}, \boldsymbol{\lambda}, \boldsymbol{\sigma}$ to ensure $\nabla\mathcal{L} = 0$. For each i^{th} time-step, the number of iterations strongly depended on the choice of the initial values. For this reason, the solution convergence (i.e., the computational time) at each t_i was promoted setting the starting configuration equal to the optimal values at t_{i-1}. This was allowed considering the continuity of the joint angles between two consecutive time-steps.

To understand the influence of $\boldsymbol{g}_1$ and $\boldsymbol{g}_2$ on the results, please refer to a simplifying example in Appendix A.

C. EXPERIMENTAL SETUP AND PROTOCOL

To prove the feasibility of the proposed optimization method, experiments were conducted on one healthy subject (29 y.o., male and BMI = 23.4 kg/m^2) in the movement analysis Polito^{BIO} Med Lab of the Politecnico di Torino (Turin, Italy). The participant provided informed consent (ethics approval prot. 474/CE 2024). The anthropometric measurements were acquired with a caliper and amounted to $l_{UA} = 0.3$ m, $l_{FA} = 0.3$ m, $2h = 0.06$ m and $\delta = 6$ deg, $\vartheta_5 \approx 20$ deg manually measured with a goniometer when the elbow was fully extended. The subject was equipped with two 3D-printed plastic supports on the UA and FA (Figure 3a). Each support hosted a MIMU and four retroreflective passive markers ($\emptyset$ = 14 mm). In detail, each support was designed with four slots to ensure the accurate alignment of three local coordinate systems: markers (green), MIMU (red), and support (blue). The supports were mounted on the subject's segments by means of Velcro straps (Figure 3b) taking care to manually align the axes of the support with the UA and FA axes. To enable a proper comparison between the MIMU and SP kinematics, two additional markers were placed on the subject's left and right acromion process (Figure 3c), to compute the time-invariant orientation between the SP and MIMU coordinate systems.

The subject was equipped with two MIMUs (Xsens – MTw, Movella, Enschede, The Netherlands, sampling frequency = 100 Hz), attached to UA and FA. Noise characteristics of the MIMUs are reported in Appendix B. The SP system was composed of twelve infrared cameras (VICON - Vero, UK, sampling frequency = 100 Hz) synchronized with the MIMU station via cables.

An initial warm-up period of ten minutes was executed to limit the temperature influence on the gyroscope readings [42], [43]. After that, a static acquisition of one minute was recorded to compute the bias of each gyroscope to be removed from the angular velocity readings collected during the actual experiments. The subject was asked to sit in front of a table, first assuming an initial neutral position for a few seconds (Figure 3b), and then performing a dynamic task for ten minutes without pauses. The subject was also asked to maintain the trunk still for the whole dynamic task. The task consisted of drawing an X-shape figure with a pencil as shown in Figure 4. The trajectories of the elbow and wrist were constrained to remain within two volumes of 0.25 × 0.25 × 0.15 m and 0.33 × 0.22 × 0.10 m for elbow and wrist, respectively, as shown and discussed further on in Figure 6.

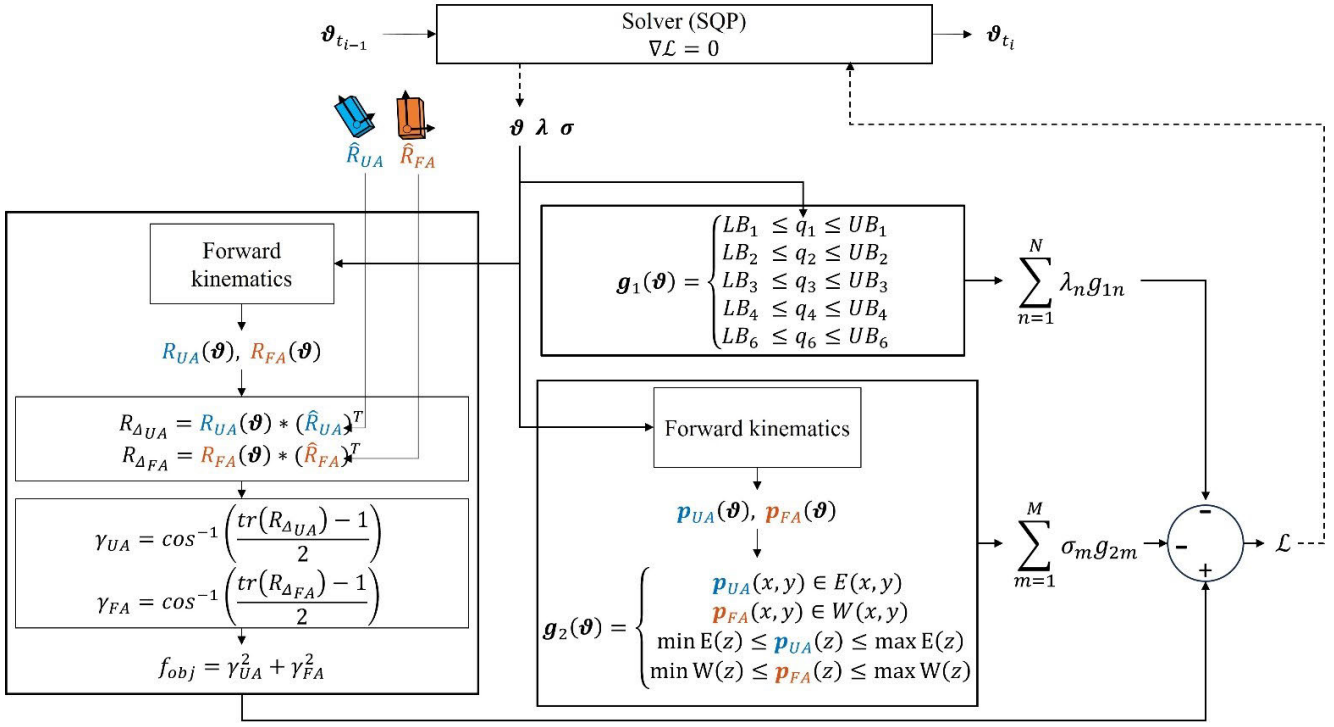

FIGURE 2. The designed real-time optimization method. Quantities with ^symbol refer to sensor fusion-based orientation. Blue and red colors refer to orientation and position of the upper arm and forearm, respectively. Dashed arrows refer to input/output quantities internal to the solver. When no constraints are applied $\lambda = \sigma = 0$ and ϑ^{un} is obtained. When constraints are applied both λ and σ can be non-zero and ϑ^{con} is obtained.

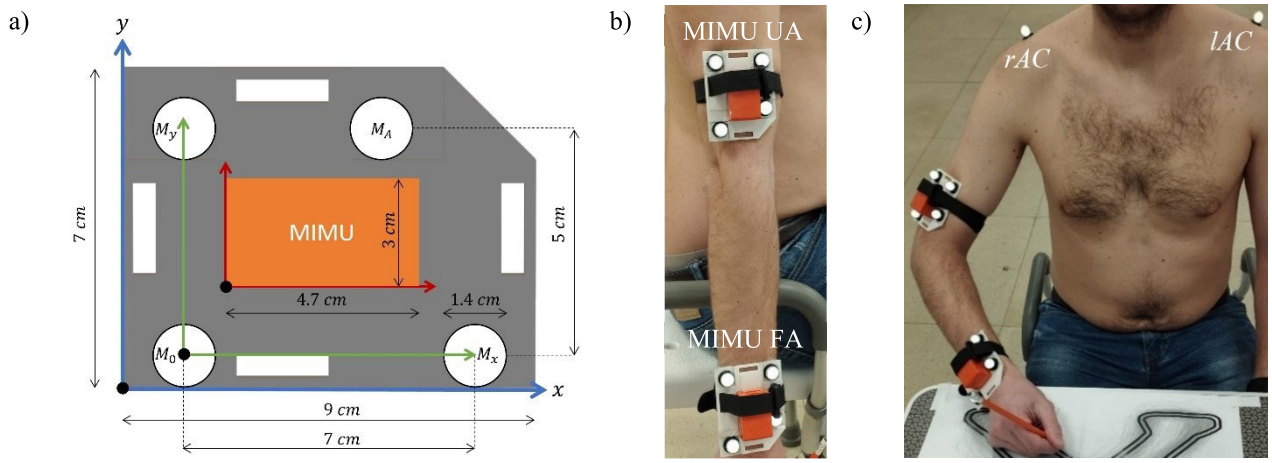

FIGURE 3. a) The plastic support equipped with four SP markers hosted in the dedicated slots and one MIMU. The local coordinate system of the support, markers, and MIMU are represented in blue, green, and red, respectively; b) the two supports aligned with the UA and FA axes; c) frontal representation of the subject equipped with the two additional markers on the left and right acromion.

D. MIMU AND SP ORIENTATION ESTIMATION

The orientation of the MIMUs mounted on the UA and FA was evaluated with respect to the global reference frame (x_0, y_0, z_0) in quaternion form using the popular and open-access sensor fusion filter by Madgwick et al. [44]. The orientations of the MIMUs were initialized using the inclination algebraic quaternion described in [45] during the neutral position at the beginning of the experiment (Figure 3b), where both the UA and FA were aligned on the horizontal plane (i.e., their z-axes were parallel and horizontal). Finally, the time-series orientation of the two MIMUs was converted into rotation matrices $\hat{R}_{UA}$ and $\hat{R}_{FA}$.

It is recognized that the filter parameter value β has a great impact on the accuracy of the orientation estimates [46], [47], [48]. For this reason, the value of β^*_{UA} and β^*_{FA}, used to compute $\hat{R}_{UA}$ and $\hat{R}_{FA}$ respectively, was estimated following the rigid-constraint-method described in [42] and [49] and detailed in Appendix C.

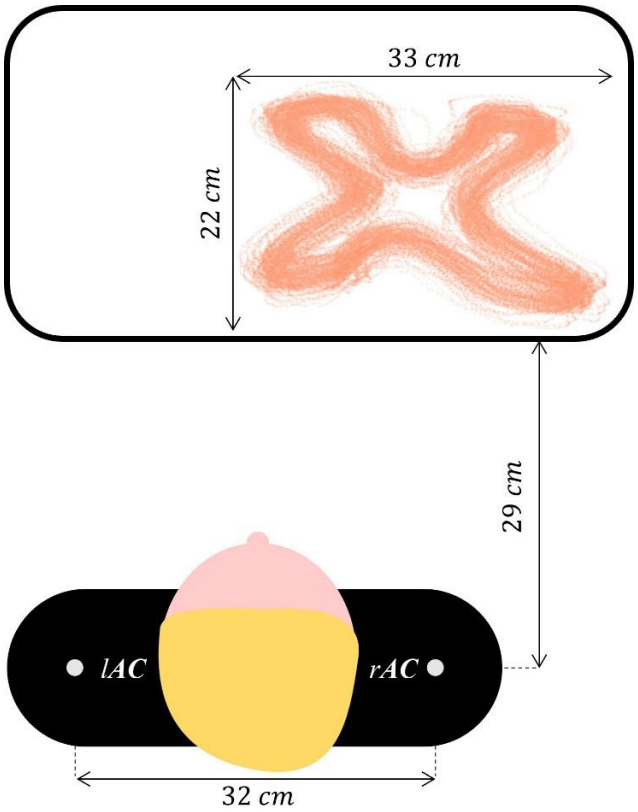

FIGURE 4. Top view of the subject in front of the table with the followed curvilinear path as reconstructed with SP system after the ten minutes experiment. The two grey circles represent the markers on the left and right acromia.

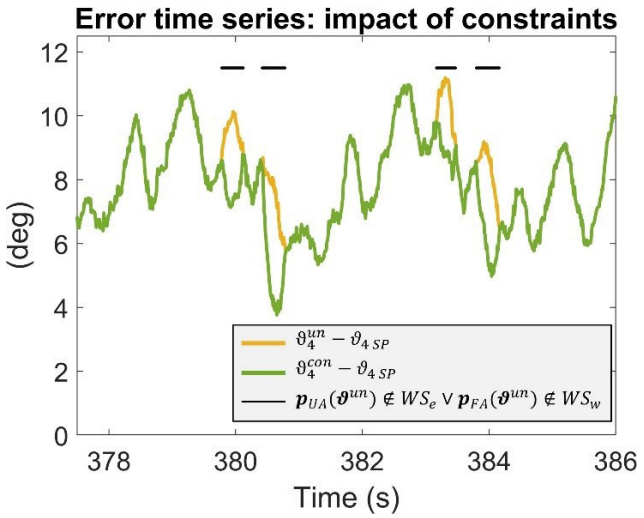

FIGURE 5. The unconstrained (yellow) vs constrained (green) error time-series of the elbow flexion-extension angle. The time intervals in which the unconstrained trajectories of the elbow and wrist joint centers fell outside the workspace boundaries (t_{out}) are represented as horizontal black lines.

The reference SP orientations for both UA and FA ($\hat{R}_{UA_{SP}}$ and $\hat{R}_{FA_{SP}}$) were computed from the marker clusters using the SVD techniques [50] and exploiting the alignment between the axes of markers and MIMUs (Figure 3a) [48]. This enabled a proper comparison between the MIMUs and SP-based joint angles.

E. DATA ANALYSIS

The optimization method was implemented in MATLAB R2022b (The MathWorks Inc., Natick, MA, USA). The values for lower and upper joint limits required in (6) were set equal to those listed in Table 1. The elbow and wrist workspace boundaries required in (7) were set equal to the size of the rectangular parallelepiped described in paragraph C.

The optimization method was run to estimate the shoulder and elbow angles starting from $\hat{R}_{UA}$ and $\hat{R}_{FA}$ without and with applying the constraints $\boldsymbol{g}_1$ and $\boldsymbol{g}_2$ to obtain $\boldsymbol{\vartheta}^{un}$ and $\boldsymbol{\vartheta}^{con}$, respectively. By applying the DH forward kinematics equations, the corresponding joint center positions $\boldsymbol{p}_{UA}(\boldsymbol{\vartheta}^{un})$, $\boldsymbol{p}_{FA}(\boldsymbol{\vartheta}^{un})$ and $\boldsymbol{p}_{UA}(\boldsymbol{\vartheta}^{con})$, $\boldsymbol{p}_{FA}(\boldsymbol{\vartheta}^{con})$ were obtained. The minimization problem was initialized with the neutral configuration [0, 0, 0, 0, ϑ_5, 0].

To perform a consistent comparison, the corresponding reference joint angles $\boldsymbol{\vartheta}_{SP}$ were obtained by running the optimization method from $\hat{R}_{UA_{SP}}$ and $\hat{R}_{FA_{SP}}$.

The average execution time for a single iteration of the optimization process was measured for an Intel® Core™ i7-10510U CPU @ 1.80 GHz in Microsoft™ Windows 11 when processing a dataset of about 62000 samples, without executing any other applications. This calculation was repeated when computing $\boldsymbol{\vartheta}^{un}$ and $\boldsymbol{\vartheta}^{con}$, separately.

F. ERROR METRICS

Four errors were computed:

- $\boldsymbol{e}_{tot}^{un} = rms(\boldsymbol{\vartheta}^{un} - \boldsymbol{\vartheta}_{SP})$, to quantify the errors on the whole recording without applying any constraints.
- $\boldsymbol{e}_{tot}^{con} = rms(\boldsymbol{\vartheta}^{con} - \boldsymbol{\vartheta}_{SP})$, to quantify the errors on the whole recording by applying the constraints.
- $\boldsymbol{e}_{out}^{un} = rms\,(\boldsymbol{\vartheta}^{un}(t_{out}) - \boldsymbol{\vartheta}_{SP}(t_{out}))$, where $t_{out} = \forall t_i \,|\, \boldsymbol{p}_{UA}(\boldsymbol{\vartheta}^{un}) \notin WS_e \vee \boldsymbol{p}_{FA}(\boldsymbol{\vartheta}^{un}) \notin WS_w$ to quantify the errors only in the time intervals in which the elbow and wrist joint centers fell outside their workspace boundaries, without applying any constraints.
- $\boldsymbol{e}_{out}^{con} = rms\,(\boldsymbol{\vartheta}^{con}(t_{out}) - \boldsymbol{\vartheta}_{SP}(t_{out}))$, to quantify the decrease of the errors due to the application of constraints, in the same time intervals of $\boldsymbol{e}_{out}^{un}$.

The $\boldsymbol{e}_{tot}^{un}$, $\boldsymbol{e}_{tot}^{con}$, $\boldsymbol{e}_{out}^{un}$, and $\boldsymbol{e}_{out}^{con}$ were a 5×1 vectors, each entry summarizing the corresponding joint angular error.

III. RESULTS

To assess the influence of constraints on the angular values, a graphical comparison between the error time-series of ϑ_4^{un} and ϑ_4^{con} is depicted in Figure 5, along with the time intervals in which the elbow and wrist joint centers fell outside their workspace boundaries. The first two panels of Figure 6

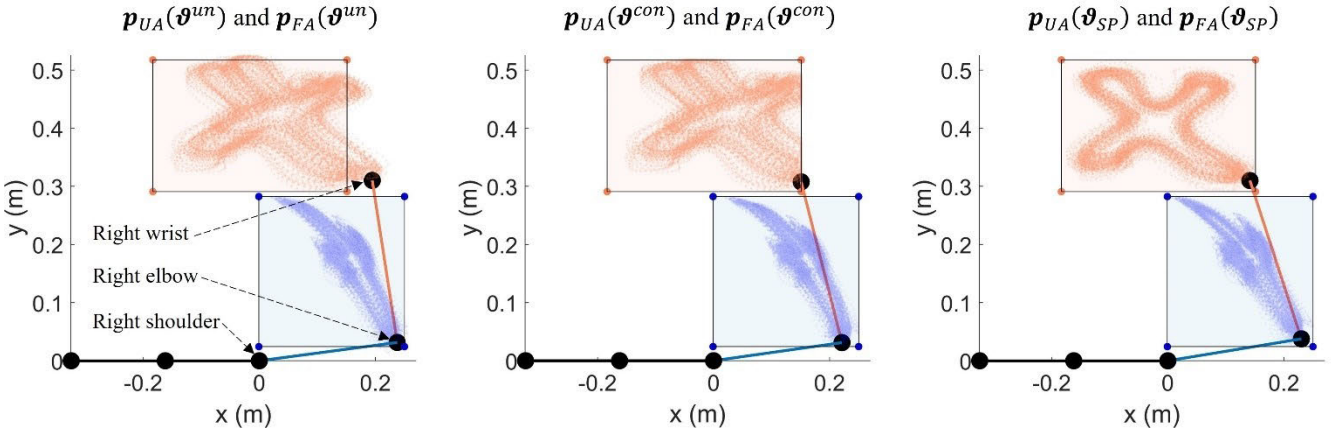

FIGURE 6. Top view reconstruction of the elbow (blue) and wrist (orange) trajectories for the entire recording when starting from the unconstrained (left), constrained (center), and reference (right) time series of the joint angles, respectively. The horizontal projection of the elbow and wrist workspaces are represented in light blue and light orange.

TABLE 2. The error metrics for the shoulder and elbow angles.

		e_{tot}^{un}	e_{tot}^{con}	e_{out}^{un}	e_{out}^{con}
Shoulder	Plane of elevation	4.0	3.9	4.7	3.7
	Elevation	3.3	3.3	4.6	3.3
	Intra-extra rotation	2.1	2.0	2.7	2.4
Elbow	Flexion-extension	6.5	6.3	8.8	7.5
	Prono-supination	3.4	3.1	5.2	4.3

Units are in degrees.

show the constraint influence on the corresponding unconstrained and trajectories, $\boldsymbol{p}_{UA}(\boldsymbol{\vartheta}^{un})$, $\boldsymbol{p}_{FA}(\boldsymbol{\vartheta}^{un})$ and $\boldsymbol{p}_{UA}(\boldsymbol{\vartheta}^{con})$, $\boldsymbol{p}_{FA}(\boldsymbol{\vartheta}^{con})$, respectively, while the third panel shows the reference trajectories.

The $\boldsymbol{e}_{tot}^{un}$, $\boldsymbol{e}_{tot}^{con}$, $\boldsymbol{e}_{out}^{un}$, and $\boldsymbol{e}_{out}^{con}$ are listed in Table 2.

The t_{out} amounted to 12.8% with respect to the total recording duration. The percentage decrease of $\boldsymbol{e}_{out}^{con}$ values with respect to $\boldsymbol{e}_{out}^{un}$ amounted to 21.3%, 28.3%, 11.1%, 14.8%, and 17.3%, for the shoulder and elbow angles.

The execution time for a single iteration amounted to 6.9 ± 0.4 ms and 11.3 ± 0.1 ms when computing $\boldsymbol{\vartheta}^{un}$ and $\boldsymbol{\vartheta}^{con}$, respectively.

IV. DISCUSSIONS

The goal of this study was to present a real-time optimization method for joint kinematics estimation based on a multi-body kinematic model for imposing subject and task specific kinematic constraints. The kinematic model was consistent with the ISB standards to enable clinical interpretability and comparison with previous studies [23], [25].

A three-segment upper limb model was defined according to DH convention.

The main feature of the proposed method is the possibility to easily and directly incorporate two different types of constraints, thus avoiding joint angles to exceed the physiological limits and producing joint kinematic outputs that guarantee for joint centers trajectories compatible with the task-specific workspace boundaries. Constraints were mathematically specified with ad hoc functions and added to the objective function to be minimized by means of the Lagrangian multipliers [51]. When no constraints were applied, errors computed over the whole recording ($\boldsymbol{e}_{tot}^{un}$) are comparable with findings from a study with a shorter duration and pauses [11] (Table 2). It is worth highlighting that constraints were active only during those time intervals in which the joint center trajectories would fall outside the workspace boundaries or when joint angles reached their limits. This situation happened for only 12.8% of the experiment's duration explaining why the reduction in angular error across the entire recording is neglectable ($\boldsymbol{e}_{tot}^{con}$ vs $\boldsymbol{e}_{tot}^{un}$). Differently, when comparing the errors only in these time intervals ($\boldsymbol{e}_{out}^{con}$ vs $\boldsymbol{e}_{out}^{un}$), an average percentage decrease of 18.5% can be appreciated when applying the constraints. To assess the influence of noise characteristics of different MIMUs on the constraints' efficacy, the reader is referred to Appendix B in which two additional repetitions were recorded and analyzed.

An important point of attention of the constraint application is that, when the constraints are not active, there is no difference between the unconstrained and constrained angles time-series, as illustrated in Figure 5. The same considerations apply to the trajectories. When no constraints were applied, the errors jeopardizing $\hat{R}_{UA}$ and $\hat{R}_{FA}$ directly affected the elbow and wrist trajectories, which exceeded the spatial boundaries defined for the experiments (left panel of Figure 6). However, with $\boldsymbol{g}_2$ applied $\boldsymbol{p}_{FA}(\boldsymbol{\vartheta}^{con})$ was more like a cropped version of the corresponding unconstrained one, rather than matching the reference shape shown in the right panel.

The task-specific constraint $\boldsymbol{g}_2$ could be generally formulated by means of linear or nonlinear functions of $\boldsymbol{\vartheta}$ to incorporate the *a-priori* knowledge of the performed movement. In this work, the joint center trajectories were forced to remain within their corresponding expected boundaries. In other cases, such as in robot-assisted rehabilitation, when

the hand moves along predefined trajectories, $\boldsymbol{g}_2$ could be set to mathematically define task-consistent joint angles. In general, the results accuracy will be highly influenced by the range of the space actually restricted by $\boldsymbol{g}_2$.

The main limit of the proposed multi-segmental model consists in the fact that the pose of the base segment needs to be known for each instant to fully reconstruct the kinematic chain via the DH equations. In our experiments, this problem was bypassed by instructing the participant to maintain his trunk still, thereby ensuring that assuming it as fixed did not markedly affect the results' accuracy. If trunk movement occurred, the suggested upper limb model would require incorporating one or more additional links to be equipped with MIMUs based on the number of segments used to describe such motion. Furthermore, it is expected that errors in the segment lengths will affect the accuracy of the joint positions, as common for mechanisms such as robots [52], [53].

Another key feature of the proposed optimization method is that it can be easily modified to incorporate additional available kinematics information. For instance, the trajectory of a joint center or the end effector could be provided using an optical system [54], [55] while the drift-free coordinates of a body segment or the mutual distance between body segments might be obtained from barometric and distance sensors, respectively [56], [57].

Finally, a further benefit was represented by the possibility of obtaining the optimized solutions in real-time, being the execution time for a single iteration lower than or almost equal to the sampling period. This was achieved despite the inherent complexity of the task and absence of explicit solutions, highlighting the efficiency and effectiveness of the optimization method.

V. CONCLUSION

This study proposed a method to estimate ISB-consistent angles in real-time compatible with the functional anatomy and the performed task, thanks to the application of reasonable constraints. When active, the constraints allowed an 18.5% reduction of the angular errors, while simultaneously avoiding unfeasible joint configurations. This method was not conceived to correct sensor-fusion errors but to reduce their impact on the final kinematics reconstruction sensor-driven data.

APPENDIX A
CONSTRAINT INFLUENCE: PLANAR EXAMPLE

As an example, consider a simple case in which the elbow and the wrist move only on the horizontal plane at the same height of the shoulder (i.e., $\vartheta_2 = 90$ deg), as shown in the top panels of Figure 7. For simplicity, consider $\delta = 0$ deg and $\vartheta_3 = \vartheta_5 = \vartheta_6 = 0$ deg. In this situation, only ϑ_1 and ϑ_4 have an impact on the results. The modelled UA and FA orientation, $R_{UA}(\vartheta_1, \vartheta_4)$ and $R_{FA}(\vartheta_1, \vartheta_4)$ can be obtained by applying the DH forward kinematics equations as in (9). For sake of clarity, the dependency of the modelled quantities on

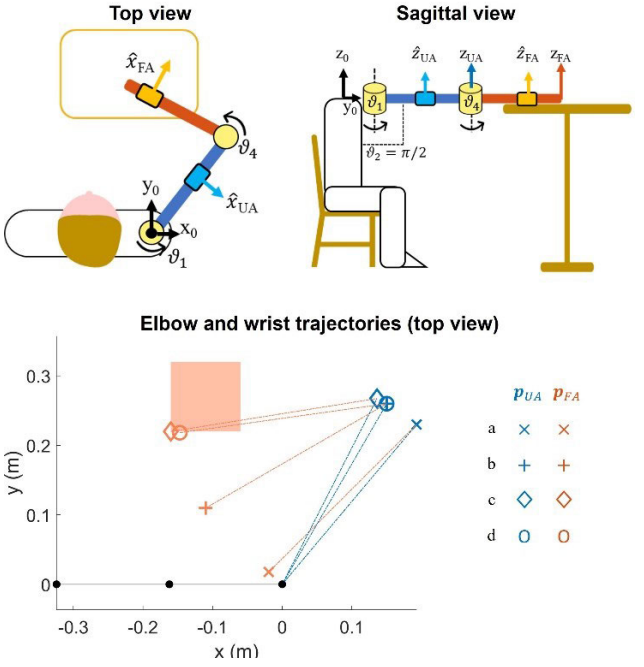

FIGURE 7. Top panels) top and sagittal views of the simplified setup. Bottom panel) comparison of p_{UA} and p_{FA} resulting from the ϑ_1 and ϑ_4 values computed in case a, b, c, and d. Each case is represented using a different marker. Elbow positions are represented in blue, while wrist positions are in orange. The wrist workspace is represented with the colored rectangular region. Note that the elbow positions for case b and d are superimposed.

$(\vartheta_1, \vartheta_4)$ in the equations is omitted for the modelled variables.

$$R_{UA} = \begin{bmatrix} \sin(\vartheta_1) & \cos(\vartheta_1) & 0 \\ -\cos(\vartheta_1) & \sin(\vartheta_1) & 0 \\ 0 & 0 & 1 \end{bmatrix}$$
$$R_{FA} = \begin{bmatrix} \sin(\vartheta_1 + \vartheta_4) & \cos(\vartheta_1 + \vartheta_4) & 0 \\ -\cos(\vartheta_1 + \vartheta_4) & \sin(\vartheta_1 + \vartheta_4) & 0 \\ 0 & 0 & 1 \end{bmatrix} \quad (9)$$

In this setup, on a given time-step, the orientations provided by the sensor fusion algorithm, $\hat{R}_{UA}$ and $\hat{R}_{FA}$, can be interpreted as elementary rotations around the z-axis of the trunk coordinate system with an angle equal to $\hat{\varphi}_{UA}$ and $\hat{\varphi}_{FA}$, respectively, as reported in (10).

$$\hat{R}_{UA} = \begin{bmatrix} \cos(\hat{\varphi}_{UA}) & -\sin(\hat{\varphi}_{UA}) & 0 \\ \sin(\hat{\varphi}_{UA}) & \cos(\hat{\varphi}_{UA}) & 0 \\ 0 & 0 & 1 \end{bmatrix}$$
$$\hat{R}_{FA} = \begin{bmatrix} \cos(\hat{\varphi}_{FA}) & -\sin(\hat{\varphi}_{FA}) & 0 \\ \sin(\hat{\varphi}_{FA}) & \cos(\hat{\varphi}_{FA}) & 0 \\ 0 & 0 & 1 \end{bmatrix} \quad (10)$$

After applying (2) and (3), the $f_{obj}(\vartheta_1, \vartheta_4)$, whose general expression is reported in (4), can be thus simplified as follows:

$$f_{obj} = \left(\vartheta_1 - \frac{\pi}{2} - \hat{\varphi}_{UA}\right)^2 + \left(\vartheta_1 + \vartheta_4 - \frac{\pi}{2} - \hat{\varphi}_{FA}\right)^2 \quad (11)$$

The constraint functions are specified in (12). In particular, $\boldsymbol{g}_2(\vartheta_1, \vartheta_4)$ was defined to ensure the wrist lies within

TABLE 3. Values of f_{obj}, ϑ_1, ϑ_4, λ, and σ for each of the four cases.

	f_{obj}	ϑ_1	ϑ_4	λ_1	λ_2	λ_3	λ_4	σ_1	σ_2	σ_3	σ_4
a	0	50	175	0	0	0	0	0	0	0	0
b	0.10	60	150	0	10	0	30	0	0	0	0
c	0.45	63	126	0	0	0	0	0	29	0	247
d	0.46	60	128	0	18	0	0	0	0	0	251

$[f_{obj}] = rad^2$, $[\vartheta_1] =$ deg, $[\vartheta_4] =$ deg. $\hat{\varphi}_{UA} = -40$ deg, $\hat{\varphi}_{FA} = 130$ deg.

a horizontal rectangle with zero height, as actually happens during this example:

$$\boldsymbol{g}_1 = \begin{cases} -\frac{\pi}{2} \leq \vartheta_1 \leq \frac{\pi}{3} \\ 0 \leq \vartheta_4 \leq \frac{5}{6}\pi \end{cases}$$
$$\boldsymbol{g}_2 = \begin{cases} -0.16 \leq p_{FA}(x) \leq -0.06 \\ 0.22 \leq p_{FA}(y) \leq 0.32 \end{cases} \quad (12)$$

According to (12) there are 8 inequalities, which means that the multipliers $\boldsymbol{\lambda}$ and $\boldsymbol{\sigma}$ contained in (8) are a 4×1 vector each. The expression of $\boldsymbol{p}_{FA}(\vartheta_1, \vartheta_4)$ can be easily obtained:

$$\boldsymbol{p}_{FA} = \begin{cases} l_{UA}\cos(\vartheta_1) + l_{FA}\cos(\vartheta_1 + \vartheta_4) \\ l_{UA}\sin(\vartheta_1) + l_{FA}\sin(\vartheta_1 + \vartheta_4) \\ 0 \end{cases} \quad (13)$$

The solutions for ϑ_1, ϑ_4, $\boldsymbol{\lambda}$, and $\boldsymbol{\sigma}$ are computed for the following four cases: a) without applying $\boldsymbol{g}_1$ and $\boldsymbol{g}_2$, b) by applying only $\boldsymbol{g}_1$, c) by applying only $\boldsymbol{g}_2$, and d) by applying both $\boldsymbol{g}_1$ and $\boldsymbol{g}_2$. The results, together with the residual optimization values f_{obj} are reported in Table 3. For all the cases $\hat{\varphi}_{UA}$ and $\hat{\varphi}_{FA}$ amounted to -40 deg and 135 deg, respectively.

From the results listed in Table 3 it is possible to assess that the $(\vartheta_1, \vartheta_4)$ values are different in a, b, c, and d. Moreover, the residual is null when no constraints are applied, as expected in case 1. In this case, the model completely adapts to $\hat{R}_{UA}$ and $\hat{R}_{FA}$ thus reflecting any sensor fusion error which may affect the two orientations. On the contrary, the residual is highest when both $\boldsymbol{g}_1$ and $\boldsymbol{g}_2$ are applied, this means that the corresponding $(\vartheta_1, \vartheta_4)$ values are certainly different with respect to case 1. It is also worth observing that, in cases 2, 3 and 4 the $\lambda_1, \lambda_3, \sigma_1$, and σ_3 values are always null. This situation is referred to "inactive constraints", meaning that the associated constraints do not actively contribute to determining the optimal solution. In other words, the obtained $(\vartheta_1, \vartheta_4)$ values automatically satisfy the constraints associated with $\lambda_1, \lambda_3, \sigma_1$, and σ_3. This usually happens when the solution is constrained between within a specific range, as in (12). Consequently, the solution can approach only one of the extremities, making inactive the constraints related to the opposite one.

The bottom panel of Figure 7 graphically represents the $\boldsymbol{p}_{UA}$ and $\boldsymbol{p}_{FA}$ resulting from the DH forward kinematics equations using the ϑ_1 and ϑ_4 values computed in the four cases (each case is represented with a different marker symbol). It is possible to observe that constrained wrist position in cases c and d largely differ from the unconstrained in case a. This is possible thanks to the effect of $\boldsymbol{g}_2$. In fact, $\hat{\varphi}_{UA}$ and $\hat{\varphi}_{FA}$ can be in general affected by errors which can be limited by applying the *a-priori* knowledge of the performed motion.

APPENDIX B
INFLUENCE OF MIMU NOISE CHARACTERISTICS

Two additional repetitions were recorded on the same subject using two additional MIMUs of the same model whose noise characteristics are reported in Table 4. The noise density, bias instability, and random walk were quantified from the Allan variance during an eight-hour static acquisition [58], while the bias residual was obtained by subtracting the mean gyroscope value from one-minute static recording acquired before and after the experiment.

TABLE 4. The noise characteristics of the employed MIMUs.

Noise Density ($\times 10^{-3}$)		Bias Instability ($\times 10^{-3}$)		Random Walk ($\times 10^{-5}$)		Bias Residual ($\times 10^{-3}$)
acc $\left(\frac{m}{s^2\sqrt{Hz}}\right)$	gyr $\left(\frac{deg}{s\sqrt{Hz}}\right)$	acc $\left(\frac{m}{s^2}\right)$	gyr $\left(\frac{deg}{s}\right)$	acc $\left(\frac{m}{s^2\sqrt{Hz}}\right)$	gyr $\left(\frac{deg}{s\sqrt{Hz}}\right)$	gyr $\left(\frac{deg}{s}\right)$
1.2	6.4	1.0	4.2	12.7	13.3	[-1 -23 -73]
1.2	6.3	1.5	2.3	4.5	15.7	[-91 -5 -51]
1.2	6.2	0.8	2.7	3.6	23.9	[-158 -61 71]
1.1	6.5	0.8	2.1	4.4	19.0	[-19 19 -40]

Each row refers to one MIMU. Rep I was recorded with MIMUs #1 and #2, Rep II with MIMUs #1 and 4, Rep III with MIMUs #3 and 2.

The metrics described in section III were also computed for rep II and rep III including e^{un}_{tot}, e^{con}_{tot}, e^{un}_{out}, e^{con}_{out}, and t_{out} and reported in Table 5.

TABLE 5. The error metrics for rep ii and rep iii.

	Rep II				Rep III			
	e^{un}_{tot}	e^{con}_{tot}	e^{un}_{out}	e^{con}_{out}	e^{un}_{tot}	e^{con}_{tot}	e^{un}_{out}	e^{con}_{out}
ϑ_1	2.5	2.5	2.6	2.1	2.3	2.3	1.9	2.1
ϑ_2	1.1	1.1	0.9	0.9	1.9	1.9	2.8	2.7
ϑ_3	3.2	3.2	3.5	3.0	2.9	2.8	5.3	4.5
ϑ_5	2.6	2.6	4.6	4.2	6.4	6.3	11	10
ϑ_6	1.9	1.9	2.7	2.6	2.5	2.5	3.3	3.1

The t_{out} for rep II and rep III amounted to 0.8% and 4.8% with respect to the total recording duration. The average percentage decrease of $\boldsymbol{e}^{con}_{out}$ values with respect to $\boldsymbol{e}^{un}_{out}$ amounted to 9.2% and 4.7% for rep II and rep III, respectively. These additional results confirm the benefits of applying constraints in reducing joint angle errors. Although the movement was the same as in repetition I, it is noteworthy that both t_{out} and the average percentage decrease varied considerably among the three repetitions. These variations are primarily due to the different noise characteristics of the MIMUs, as shown in Table 4 where it is evident that the bias residual is the most fluctuating characteristic, consistently with literature findings [48]. This remarks the fact that different MIMUs, even from the same model, may provide different performance, including the instants at which the elbow and wrist joint centers fell outside the workspace limits.

Employing constraints can help minimize these variations, making the results more consistent and repeatable.

APPENDIX C
SENSOR FUSION PARAMETER VALUE ESTIMATION

Recent literature highlighted the significance of custom tuning in sensor fusion algorithms to account for noise characteristics of both MIMU models and movement kinematics, since default parameter values provided in filter implementations may lead to substantial errors [48]. The optimal parameter value is defined as the one which minimizes the orientation error with respect to the reference. However, relying on a known orientation reference is impractical for home monitoring, which is the focus of this study. To set a reasonable parameter value without using any reference, this work adopted the ''rigid-constraint method'' (RCM, [42], [49]). The RCM, applied to two aligned MIMUs on a rigid body, identifies the parameter value minimizing the difference between the orientation independently estimated by each MIMU, following a grid-search approach.

For this reason, two MIMUs of the same model were rigidly stacked and aligned with the UA and FA axes of the DH model, respectively, as depicted in Figure 8. Then, a preliminary exercise similar to that described in Paragraph C. was executed, as suggested in [49].

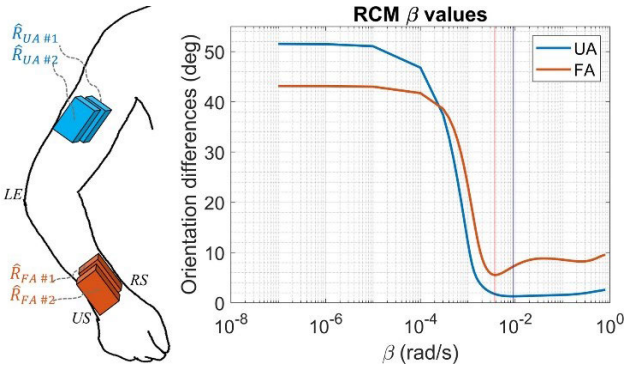

FIGURE 8. Left) the setup for rigid constraint methods used for the preliminary experiments aimed at estimating β^*_{UA} and β^*_{FA}. Right) the relative orientation difference for each value of β for the MIMU pairs mounted on the upper arm (in blue) and on the forearm (in orange), respectively.

After that, the RCM was applied to UA and FA MIMU pairs, independently. To this end, the orientation of each of the four MIMUs, separately, was computed with the Madgwick's filter for 77 values in the range $\boldsymbol{\beta} = [0, 0.8]$ rad/s to obtain $\hat{R}_{UA\#1}(\boldsymbol{\beta})$, $\hat{R}_{UA\#2}(\boldsymbol{\beta})$, $\hat{R}_{FA\#1}(\boldsymbol{\beta})$, and $\hat{R}_{FA\#2}(\boldsymbol{\beta})$, respectively. The suitable value for each pair of MIMUs, β^*_{UA} and β^*_{FA}, were obtained as follows:

$$\begin{aligned}\beta^*_{UA} &= \beta | \min f_{AA}\left(\hat{R}_{UA\#1}(\boldsymbol{\beta})^T \hat{R}_{UA\#2}(\boldsymbol{\beta})\right)\\ \beta^*_{FA} &= \beta | \min f_{AA}\left(\hat{R}_{FA\#1}(\boldsymbol{\beta})^T \hat{R}_{FA\#2}(\boldsymbol{\beta})\right)\end{aligned} \tag{14}$$

where f_{AA} is the function to extract the angular value after the conversion of the matrix into its axis-angle representation, as in (3). The identified β^*_{UA} and β^*_{FA} amounted to 0.0091 rad/s and 0.0037 rad/s, respectively. The chart depicted in Figure 8 shows the trend of the relative orientation difference when varying β for each pair of MIMU, β^*_{UA} and β^*_{FA} are also highlighted. Finally, β^*_{UA} and β^*_{FA} were used to compute $\hat{R}_{UA}$ and $\hat{R}_{FA}$ during the actual experiments described in Paragraph II-C.

For the sake of completeness, since the main setup included the markers aligned with the MIMU axes (Figure 3), the absolute orientation error corresponding to $\hat{R}_{UA}$ and $\hat{R}_{FA}$ was also assessed as described in [49] and amounted to 2.8 deg and 10.8 deg, respectively. The higher errors for $\hat{R}_{FA}$ can be attributed to the increased motion intensity of the FA compared to the UA [48]. More in detail, the maintenance of the elbow flexion-extension axis nearly vertical during the task made it difficult to effectively compensate the drift on the horizontal plane. While the magnetometer theoretically addresses this issue, it introduces its own set of problems [42]. It is work noting that despite the 10-minute duration, the RCM served as one viable approach to provide parameter values to contain the absolute orientation errors within reasonable limits in a home-setting without relying on any orientation reference.

APPENDIX D
CODE AND DATA SHARING

Code and data associated with this article are available on CodeOcean 10.24433/CO.2174974. Two main MATLAB scripts are provided, one is an interactive script for the movement visualization with the designed upper limb model, the second is the script to run the proposed optimization method.

GLOSSARY

The main symbols used in this manuscript are listed below:

$d_j, a_j, \theta_j, \alpha_j$	Parameters of the DH model.
$\boldsymbol{\vartheta}$	Generic vector (6×1) of the upper limb angles.
$\vartheta_1, \vartheta_2, \vartheta_3$	Generic shoulder angles.
$\vartheta_4, \vartheta_5, \vartheta_6$	Generic elbow angles. ϑ_5 represents the carrying angle and is fixed and subject specific.
$\boldsymbol{p}_{TR}(\boldsymbol{\vartheta})$ $\boldsymbol{p}_{UA}(\boldsymbol{\vartheta})$ $\boldsymbol{p}_{FA}(\boldsymbol{\vartheta})$	Generic position vectors (3×1) for the trunk, upper arm, and forearm joint centers, respectively after applying the DH forward kinematics equations.
δ	The rotation required to properly center the forearm axes, based on the assumption of the forearm as a planar trapezium.
(x_0, y_0, z_0) (x_3, y_3, z_3) (x_6, y_6, z_6)	Coordinate system axes for the trunk, upper arm, and forearm, respectively.
$R_{UA}(\boldsymbol{\vartheta})$ $R_{FA}(\boldsymbol{\vartheta})$	Generic rotation matrices (3×3) representing the modelled UA and FA orientations after applying the DH forward kinematics equations.

$\hat{R}_{UA}$ $\hat{R}_{FA}$ Rotation matrices (3 × 3) representing the orientation of the MIMUs mounted on UA and FA obtained from a sensor fusion algorithm.

$\hat{R}_{UA_{SP}}$ $\hat{R}_{FA_{SP}}$ Rotation matrices (3 × 3) representing the reference orientations of the MIMUs mounted on UA and FA obtained from the stereophotogrammetry data. Used for validation purposes only.

γ_{UA} γ_{FA} Angular values representing the magnitude of differences between the model-based and sensor fusion-based orientations of UA and FA, respectively.

$f_{obj}(\boldsymbol{\vartheta})$ The nonlinear multivariable objective function.

$\boldsymbol{g}_1(\boldsymbol{\vartheta})$ Constraint functions applied to the optimization process to prevent joint angles from exceeding physiological ranges.

$\boldsymbol{g}_2(\boldsymbol{\vartheta})$ Constraint functions applied to the optimization process to ensure that the elbow and wrist center trajectories remain within physical workspace boundaries.

$\boldsymbol{\lambda}, \boldsymbol{\sigma}$ Lagrangian multipliers associated with the constraints $\boldsymbol{g}_1$ and $\boldsymbol{g}_2$ used to enforce the constraints during the optimization process.

$\mathcal{L}(\boldsymbol{\vartheta}, \boldsymbol{\lambda}, \boldsymbol{\sigma})$ The Lagrangian function, incorporating the objective function and the constraints.

$\beta^*_{UA}, \beta^*_{FA}$ Filter parameter values used to compute $\hat{R}_{UA}$ and $\hat{R}_{FA}$ obtained through the rigid-constraint-method described in Appendix B.

$\boldsymbol{\vartheta}^{un}$ The optimal joint angles obtained from the optimization method fed with $\hat{R}_{UA}$ and $\hat{R}_{FA}$ without applying the constraint functions $\boldsymbol{g}_1$ and $\boldsymbol{g}_2$.

$\boldsymbol{\vartheta}^{con}$ The optimal joint angles obtained from the optimization method fed with $\hat{R}_{UA}$ and $\hat{R}_{FA}$ by applying the constraint functions $\boldsymbol{g}_1$ and $\boldsymbol{g}_2$.

$\boldsymbol{\vartheta}_{SP}$ The reference joint angles obtained from the optimization method fed with $\hat{R}_{UA_{SP}}$ and $\hat{R}_{FA_{SP}}$. Used for validation purposes only.

$\boldsymbol{p}_{UA}(\boldsymbol{\vartheta}^{un})$ $\boldsymbol{p}_{FA}(\boldsymbol{\vartheta}^{un})$; $\boldsymbol{p}_{UA}(\boldsymbol{\vartheta}^{con})$ $\boldsymbol{p}_{FA}(\boldsymbol{\vartheta}^{con})$; $\boldsymbol{p}_{UA}(\boldsymbol{\vartheta}_{SP})$ $\boldsymbol{p}_{FA}(\boldsymbol{\vartheta}_{SP})$ Position vectors for elbow and wrist joint centers obtained starting from $\boldsymbol{\vartheta}^{un}$, $\boldsymbol{\vartheta}^{con}$, and $\boldsymbol{\vartheta}_{SP}$, separately.

$\mathrm{WS_e}$, $\mathrm{WS_w}$ Sets defining the workspace volumes for the elbow and wrist centers, ensuring the motion stays within predefined spatial boundaries.

t_{out} $\forall t_i | \boldsymbol{p}_{UA}(\boldsymbol{\vartheta}^{un}) \notin WS_e \vee \boldsymbol{p}_{FA}(\boldsymbol{\vartheta}^{un}) \notin WS_w$, i.e., those time intervals where the elbow and wrist exceed their workspace boundaries.

$\boldsymbol{e}^{un}_{tot}$ Errors vector (5 × 1) containing the rms of the difference between the full time series of $\boldsymbol{\vartheta}^{un}$ and $\boldsymbol{\vartheta}_{SP}$.

$\boldsymbol{e}^{con}_{tot}$ Errors vector (5 × 1) containing the rms of the difference between the full time series of $\boldsymbol{\vartheta}^{con}$ and $\boldsymbol{\vartheta}_{SP}$.

$\boldsymbol{e}^{un}_{out}$ Errors vector (5 × 1) containing the rms of the difference between $\boldsymbol{\vartheta}^{un}$ and $\boldsymbol{\vartheta}_{SP}$ evaluated at t_{out}.

$\boldsymbol{e}^{con}_{out}$ Errors vector (5 × 1) containing the rms of the difference between $\boldsymbol{\vartheta}^{con}$ and $\boldsymbol{\vartheta}_{SP}$ evaluated at t_{out}.

REFERENCES

[1] E. S. Grood and W. J. Suntay, "A joint coordinate system for the clinical description of three-dimensional motions: Application to the knee," *J. Biomechanical Eng.*, vol. 105, no. 2, pp. 136–144, May 1983, doi: 10.1115/1.3138397.

[2] A. Nez, L. Fradet, P. Laguillaumie, T. Monnet, and P. Lacouture, "Simple and efficient thermal calibration for MEMS gyroscopes," *Med. Eng. Phys.*, vol. 55, pp. 60–67, May 2018, doi: 10.1016/j.medengphy.2018.03.002.

[3] D. Unsal and K. Demirbas, "Estimation of deterministic and stochastic IMU error parameters," in *Proc. IEEE/ION Position, Location Navigat. Symp.*, Apr. 2012, pp. 862–868, doi: 10.1109/PLANS.2012.6236828.

[4] B. Kirking, "Angle measurement stability and cycle counting accuracy of hours-long duration IMU based arm motion tracking with application to normal shoulder ADLs," *Gait Posture*, vol. 100, pp. 27–32, Feb. 2023, doi: 10.1016/j.gaitpost.2022.11.020.

[5] M. Al Borno, J. O'Day, V. Ibarra, J. Dunne, A. Seth, A. Habib, C. Ong, J. Hicks, S. Uhlrich, and S. Delp, "OpenSense: An open-source toolbox for inertial-measurement-unit-based measurement of lower extremity kinematics over long durations," *J. NeuroEng. Rehabil.*, vol. 19, no. 1, p. 22, Feb. 2022, doi: 10.1186/s12984-022-01001-x.

[6] P. Slade, A. Habib, J. L. Hicks, and S. L. Delp, "An open-source and wearable system for measuring 3D human motion in real-time," *IEEE Trans. Biomed. Eng.*, vol. 69, no. 2, pp. 678–688, Feb. 2022, doi: 10.1109/TBME.2021.3103201.

[7] L. Tagliapietra, L. Modenese, E. Ceseracciu, C. Mazza, and M. Reggiani, "Validation of a model-based inverse kinematics approach based on wearable inertial sensors," *Comput. Methods Biomechanics Biomed. Eng.*, vol. 21, no. 16, pp. 834–844, Dec. 2018, doi: 10.1080/10255842.2018.1522532.

[8] B. H. W. Koning, M. M. van der Krogt, C. T. M. Baten, and B. F. J. M. Koopman, "Driving a musculoskeletal model with inertial and magnetic measurement units," *Comput. Methods Biomechanics Biomed. Eng.*, vol. 18, no. 9, pp. 1003–1013, Jul. 2015, doi: 10.1080/10255842.2013.867481.

[9] M. Begon, M. S. Andersen, and R. Dumas, "Multibody kinematics optimization for the estimation of upper and lower limb human joint kinematics: A systematized methodological review," *J. Biomechanical Eng.*, vol. 140, no. 3, pp. 1–11, Mar. 2018, doi: 10.1115/1.4038741.

[10] V. Richard, "Multi-body optimization method for the estimation of joint kinematics: Prospects of improvement," Doctoral dissertation, Dept. Mech., Univ. de Lyon, Lyon, France, 2016. [Online]. Available: https://www.researchgate.net/publication/307866702

[11] P. Picerno, P. Caliandro, C. Iacovelli, C. Simbolotti, M. Crabolu, D. Pani, G. Vannozzi, G. Reale, P. M. Rossini, L. Padua, and A. Cereatti, "Upper limb joint kinematics using wearable magnetic and inertial measurement units: An anatomical calibration procedure based on bony landmark identification," *Sci. Rep.*, vol. 9, no. 1, p. 14449, Dec. 2019, doi: 10.1038/s41598-019-50759-z.

[12] W.-W. Liao, S. McCombe Waller, and J. Whitall, "Kinect-based individualized upper extremity rehabilitation is effective and feasible for individuals with stroke using a transition from clinic to home protocol," *Cogent Med.*, vol. 5, no. 1, Jan. 2018, Art. no. 1428038, doi: 10.1080/2331205x.2018.1428038.

[13] M. Laitenberger, M. Raison, D. Périé, and M. Begon, "Refinement of the upper limb joint kinematics and dynamics using a subject-specific closed-loop forearm model," *Multibody Syst. Dyn.*, vol. 33, no. 4, pp. 413–438, Apr. 2015, doi: 10.1007/s11044-014-9421-z.

[14] J. Z. Nie, J. W. Nie, N.-T. Hung, R. J. Cotton, and M. W. Slutzky, "Portable, open-source solutions for estimating wrist position during reaching in people with stroke," *Sci. Rep.*, vol. 11, no. 1, pp. 1–13, Nov. 2021, doi: 10.1038/s41598-021-01805-2.

[15] A. Zedda, E. Gusai, M. Caruso, S. Bertuletti, G. Baldazzi, S. Spanu, D. Riboni, A. Pibiri, M. Monticone, A. Cereatti, and D. Pani, "DoMoMEA: A home-based telerehabilitation system for stroke patients," in *Proc. 42nd Annu. Int. Conf. IEEE Eng. Med. Biol. Soc. (EMBC)*, Jul. 2020, pp. 5773–5776, doi: 10.1109/EMBC44109.2020.9175742.

[16] M. Melchiorre, L. S. Scimmi, S. Mauro, and S. P. Pastorelli, "Vision-based control architecture for human–robot hand-over applications," *Asian J. Control*, vol. 23, no. 1, pp. 105–117, Jan. 2021, doi: 10.1002/asjc.2480.

[17] E. Digo, L. Gastaldi, M. Antonelli, S. P. Pastorelli, A. Cereatti, and M. Caruso, "Real-time estimation of upper limbs kinematics with IMUs during typical industrial gestures," *Proc. Comput. Sci.*, vol. 200, pp. 1041–1047, 2022, doi: 10.1016/j.procs.2022.01.303.

[18] D. Wells, J. Alderson, V. Camomilla, C. Donnelly, B. Elliott, and A. Cereatti, "Elbow joint kinematics during cricket bowling using magneto-inertial sensors: A feasibility study," *J. Sports Sci.*, vol. 37, no. 5, pp. 515–524, Mar. 2019, doi: 10.1080/02640414.2018.1512845.

[19] E. Pennestrì, A. Renzi, and P. Santonocito, "Dynamic modeling of the human arm with video-based experimental analysis," *Multibody Syst. Dyn.*, vol. 7, no. 4, pp. 389–406, May 2002, doi: 10.1023/A:1015573611400.

[20] G. Wu, F. C. T. van der Helm, H. E. J. D. Veeger, M. Makhsous, P. Van Roy, C. Anglin, J. Nagels, A. R. Karduna, K. McQuade, X. Wang, F. W. Werner, and B. Buchholz, "ISB recommendation on definitions of joint coordinate systems of various joints for the reporting of human joint motion—Part II: Shoulder, elbow, wrist and hand," *J. Biomechanics*, vol. 38, no. 5, pp. 981–992, May 2005, doi: 10.1016/j.jbiomech.2004.05.042.

[21] V. Cornagliotto, E. Digo, and S. Pastorelli, "Using a robot calibration approach toward fitting a human arm model," in *Advances in Service and Industrial Robotics*, vol. 102, S. Zeghloul, M. A. Laribi, and J. Sandoval, Eds., Cham, Switzerland: Springer, Jun. 2021, pp. 199–207, doi: 10.1007/978-3-030-75259-0_22.

[22] J. K. Aggarwal and Q. Cai, "Human motion analysis: A review," *Comput. Vis. Image Understand.*, vol. 73, no. 3, pp. 428–440, Mar. 1999, doi: 10.1006/cviu.1998.0744.

[23] A. G. Cutti, A. Giovanardi, L. Rocchi, A. Davalli, and R. Sacchetti, "Ambulatory measurement of shoulder and elbow kinematics through inertial and magnetic sensors," *Med. Biol. Eng. Comput.*, vol. 46, no. 2, pp. 169–178, Feb. 2008, doi: 10.1007/s11517-007-0296-5.

[24] M. El-Gohary and J. McNames, "Shoulder and elbow joint angle tracking with inertial sensors," *IEEE Trans. Biomed. Eng.*, vol. 59, no. 9, pp. 2635–2641, Sep. 2012, doi: 10.1109/TBME.2012.2208750.

[25] J. Yang, X. Feng, J. H. Kim, Y. Xiang, and S. Rajulu, "Joint coupling for human shoulder complex," in *Digital Human Modeling*, V. G. Duffy, Ed., Berlin, Germany: Springer, 2009, pp. 72–81.

[26] S. Parasuraman, K. C. Yee, and A. Oyong, "Human upper limb and arm kinematics for robot based rehabilitation," in *Proc. IEEE/ASME Int. Conf. Adv. Intell. Mechatronics*, Jul. 2009, pp. 845–850, doi: 10.1109/AIM.2009.5229906.

[27] A. Bertomeu-Motos, L. Lledó, J. Díez, J. Catalan, S. Ezquerro, F. Badesa, and N. Garcia-Aracil, "Estimation of human arm joints using two wireless sensors in robotic rehabilitation tasks," *Sensors*, vol. 15, no. 12, pp. 30571–30583, Dec. 2015, doi: 10.3390/s151229818.

[28] M. H. Rahman, T. K. Ouimet, M. Saad, J. P. Kenne, and P. S. Archambault, "Development and control of a wearable robot for rehabilitation of elbow and shoulder joint movements," in *Proc. 36th Annu. Conf. IEEE Ind. Electron. Soc.*, Nov. 2010, pp. 1506–1511, doi: 10.1109/IECON.2010.5675459.

[29] A. M. Zanchettin, P. Rocco, L. Bascetta, I. Symeonidis, and S. Peldschus, "Kinematic analysis and synthesis of the human arm motion during a manipulation task," in *Proc. IEEE Int. Conf. Robot. Autom.*, May 2011, pp. 2692–2697, doi: 10.1109/ICRA.2011.5979654.

[30] A. Alizadegan and S. Behzadipour, "Shoulder and elbow joint angle estimation for upper limb rehabilitation tasks using low-cost inertial and optical sensors," *J. Mech. Med. Biol.*, vol. 17, no. 2, Mar. 2017, Art. no. 1750031, doi: 10.1142/s0219519417500312.

[31] A. Arefeen and Y. Xiang, "Design human–robot collaborative lifting task using optimization," in *Proc. Int. Design Eng. Tech. Conf. Comput. Inf. Eng. Conf.*, vol. 2, Aug. 2021, p. V002T02A010, doi: 10.1115/DETC2021-71818. [Online]. Available: https://asmedigitalcollection.asme.org/IDETC-CIE/proceedings-pdf/IDETC-CIE2021/85376/V002T02A010/6801221/v002t02a010-detc2021-71818.pdf

[32] S. Glowinski and A. Blazejewski, "An exoskeleton arm optimal configuration determination using inverse kinematics and genetic algorithm," *Acta Bioeng. Biomech.*, vol. 21, no. 1, pp. 45–53, 2019, doi: 10.5277/ABB-01268-2018-02.

[33] D. Zhou, H. Wu, Z. Guo, Q. Zhou, and Y. Liang, "Maintenance accessibility evaluation method based on D-H model and comfort in a virtual maintenance environment," *Int. J. Adv. Manuf. Technol.*, vol. 121, nos. 1–2, pp. 1429–1442, Jul. 2022, doi: 10.1007/s00170-022-09432-5.

[34] R. R. Prashanna, J. Johnson, B. S. Ramesh, C. Maheswari, S. Vaisali, and S. Shankar, "Design and modelling of a human upper limb for rehabilitation exoskeleton," *J. Eng. Sci. Technol. Rev.*, vol. 17, no. 2, pp. 9–15, Apr. 2024, doi: 10.25103/jestr.172.02.

[35] B. Siciliano, L. Sciavicco, L. Villani, and G. Oriolo, "Force Control," in *Robotics: Modelling, Planning and Control* (Advanced Textbooks in Control and Signal Processing). London, U.K.: Springer-Verlag, 2009, doi: 10.1007/978-1-84628-642-1.

[36] A. Bicchi and A. Colombo, "Improved estimation of elbow flexion angle from IMU measurements using anatomical constraints," *IRBM*, vol. 45, no. 1, Feb. 2024, Art. no. 100820, doi: 10.1016/j.irbm.2024.100820.

[37] E. Digo, M. Antonelli, V. Cornagliotto, S. Pastorelli, and L. Gastaldi, "Collection and analysis of human upper limbs motion features for collaborative robotic applications," *Robotics*, vol. 9, no. 2, p. 33, May 2020, doi: 10.3390/robotics9020033.

[38] G. Rab, K. Petuskey, and A. Bagley, "A method for determination of upper extremity kinematics," *Gait Posture*, vol. 15, no. 2, pp. 113–119, Apr. 2002, doi: 10.1016/s0966-6362(01)00155-2.

[39] A. Guatibonza, C. Zabala, L. Solaque, A. Velasco, and L. Peñuela, "Mechanical design of an upper limb robotic rehabilitation system," *Int. J. Comput. Methods Eng. Sci. Mech.*, vol. 25, no. 5, pp. 265–285, May 2024, doi: 10.1080/15502287.2023.2294302.

[40] M. C. Bartholomew-Biggs, "Recursive quadratic programming methods based on the augmented Lagrangian," in *Proc. Comput. Math. Program.*, 1987, pp. 21–41, doi: 10.1007/BFb0121177.

[41] S. Nordbeck and B. Rystedt, "Computer cartography point-in-polygon programs," *BIT*, vol. 7, no. 1, pp. 39–64, Mar. 1967, doi: 10.1007/bf01934125.

[42] M. Caruso, A. M. Sabatini, M. Knaflitz, M. Gazzoni, U. D. Croce, and A. Cereatti, "Orientation estimation through magneto-inertial sensor fusion: A heuristic approach for suboptimal parameters tuning," *IEEE Sensors J.*, vol. 21, no. 3, pp. 3408–3419, Feb. 2021, doi: 10.1109/JSEN.2020.3024806.

[43] A. M. Sabatini, "Estimating three-dimensional orientation of human body parts by inertial/magnetic sensing," *Sensors*, vol. 11, no. 2, pp. 1489–1525, Jan. 2011, doi: 10.3390/s110201489.

[44] S. O. H. Madgwick, A. J. L. Harrison, and R. Vaidyanathan, "Estimation of IMU and MARG orientation using a gradient descent algorithm," in *Proc. IEEE Int. Conf. Rehabil. Robot.*, Jun. 2011, pp. 1–7, doi: 10.1109/ICORR.2011.5975346.

[45] R. Valenti, I. Dryanovski, and J. Xiao, "Keeping a good attitude: A quaternion-based orientation filter for IMUs and MARGs," *Sensors*, vol. 15, no. 8, pp. 19302–19330, Aug. 2015, doi: 10.3390/s150819302.

[46] D. Laidig, M. Caruso, A. Cereatti, and T. Seel, "BROAD—A benchmark for robust inertial orientation estimation," *Data*, vol. 6, no. 7, p. 72, Jun. 2021, doi: 10.3390/data6070072.

[47] L. Ricci, F. Taffoni, and D. Formica, "On the orientation error of IMU: Investigating static and dynamic accuracy targeting human motion," *PLoS ONE*, vol. 11, no. 9, 2016, Art. no. e0161940, doi: 10.1371/journal.pone.0161940.

[48] M. Caruso, A. M. Sabatini, D. Laidig, T. Seel, M. Knaflitz, U. D. Croce, and A. Cereatti, "Analysis of the accuracy of ten algorithms for orientation estimation using inertial and magnetic sensing under optimal conditions: One size does not fit all," *Sensors*, vol. 21, no. 7, p. 2543, Apr. 2021, doi: 10.3390/s21072543.

[49] M. Caruso, A. M. Sabatini, M. Knaflitz, U. D. Croce, and A. Cereatti, "Extension of the rigid-constraint method for the heuristic suboptimal parameter tuning to ten sensor fusion algorithms using inertial and magnetic sensing," *Sensors*, vol. 21, no. 18, p. 6307, Sep. 2021, doi: 10.3390/s21186307.

[50] A. Cappozzo, A. Cappello, U. D. Croce, and F. Pensalfini, "Surface-marker cluster design criteria for 3-D bone movement reconstruction," *IEEE Trans. Biomed. Eng.*, vol. 44, no. 12, pp. 1165–1174, Dec. 1997, doi: 10.1109/10.649988.

[51] C. Mavroidis, E. Lee, and M. Alam, "A new polynomial solution to the geometric design problem of spatial R-R robot manipulators using the denavit and hartenberg parameters," *J. Mech. Des.*, vol. 123, no. 1, pp. 58–67, Mar. 2001, doi: 10.1115/1.1335484.
[52] J. Liu, H. Ouyang, X. Han, and G. Liu, "Optimal sensor placement for uncertain inverse problem of structural parameter estimation," *Mech. Syst. Signal Process.*, vol. 160, Nov. 2021, Art. no. 107914, doi: 10.1016/j.ymssp.2021.107914.
[53] J. Zhang, F. Ding, J. Liu, L. Cao, and K. Li, "Uncertainty inverse analysis of positioning accuracy for error sources identification of industrial robots," *IEEE Trans. Rel.*, vol. 72, no. 3, pp. 1123–1133, Sep. 2023, doi: 10.1109/TR.2022.3215673.
[54] D. Balta, H. Kuo, J. Wang, I. G. Porco, O. Morozova, M. M. Schladen, A. Cereatti, P. S. Lum, and U. D. Croce, "Characterization of infants' general movements using a commercial RGB-depth sensor and a deep neural network tracking processing tool: An exploratory study," *Sensors*, vol. 22, no. 19, p. 7426, Sep. 2022, doi: 10.3390/s22197426.
[55] C. He, P. Kazanzides, H. Sen, S. Kim, and Y. Liu, "An inertial and optical sensor fusion approach for six degree-of-freedom pose estimation," *Sensors*, vol. 15, no. 7, pp. 16448–16465, Jul. 2015, doi: 10.3390/s150716448.
[56] A. M. Sabatini, G. Ligorio, A. Mannini, V. Genovese, and L. Pinna, "Prior-to- and post-impact fall detection using inertial and barometric altimeter measurements," *IEEE Trans. Neural Syst. Rehabil. Eng.*, vol. 24, no. 7, pp. 774–783, Jul. 2016, doi: 10.1109/TNSRE.2015.2460373.
[57] R. Rossanigo, M. Caruso, S. Bertuletti, F. Deriu, M. Knaflitz, U. D. Croce, and A. Cereatti, "Base of support, step length and stride width estimation during walking using an inertial and infrared wearable system," *Sensors*, vol. 23, no. 8, p. 3921, Apr. 2023, doi: 10.3390/s23083921.
[58] F. Salis et al., "A multi-sensor wearable system for the assessment of diseased gait in real-world conditions," *Frontiers Bioeng. Biotechnol.*, vol. 11, p. 518, Apr. 2023, doi: 10.3389/fbioe.2023.1143248.

MARCO CARUSO (Member, IEEE) was born in Vercelli, Italy, in 1993. He received the M.S. degree in biomedical engineering from Politecnico di Torino, Italy, in 2017, and the joint Ph.D. degree from Politecnico di Torino and the University of Turin, in 2022. His Ph.D. thesis is titled "Methods and Good Practice Guidelines for Human Joint Kinematics Estimation Through Magnetic and Inertial Wearable Sensors." He is currently an Assistant Professor (with a time contract) with the Department of Electronics and Telecommunications, Politecnico di Torino. His research interests include the use of wearable sensors, the development of sensor fusion algorithms for orientation and position estimation, and the development of biomechanical models for the real-time tracking of the human joint during rehabilitation.

ELISA DIGO received the B.S. and M.S. degrees in biomedical engineering and the Ph.D. degree in mechanical engineering (cum laude) from Politecnico di Torino, in 2016, 2018, and 2022, respectively. Since 2022, she has been a Postdoctoral Researcher with Politecnico di Torino. Thanks to the application of knowledge from mechanics and robotics to the analysis of human motion for several purposes, she developed her expertise in biomechanics. Her research interests include the use of wearable sensors for human motion analysis in different contexts, such as industry, rehabilitation, and sport.

LAURA GASTALDI received the M.S. degree in mechanical engineering, in 1993, and the Ph.D. degree in applied mechanics, in 1997. Currently, she is an Associate Professor of applied mechanics with Politecnico di Torino. She has co-authored more than 150 publications and four patents. Her research interests include biomechanics, with a focus on the analysis of sports gestures in athletes with physical disabilities, the development of sports equipment and prostheses for disabled athletes, modeling and numerical simulation of physiological systems, the development of mechanical models for human motion analysis, and human motion capture methodologies.

STEFANO PASTORELLI received the M.S. degree in mechanical engineering, in 1992, and the Ph.D. degree in applied mechanics, in 1996. He is currently a Full Professor of applied mechanics and robotics with the Department of Mechanical and Aerospace Engineering, Politecnico di Torino, Italy. He has co-authored more than 180 publications and five patents. His research interests include mechatronics for servo-actuation and mechanical power transmission, collaborative and wearable robotics, robotic systems in aerospace and service robotics, systems with physical human–machine interaction, human motion tracking, and biomechanical modeling for the development of human-centered design applications. He is a member of the International Federation for the Promotion of Mechanism and Machine Science (IFToMM) and Italian National Institute for Robotics and Intelligent Machines (I-RIM).

ANDREA CEREATTI received the M.S. degree (cum laude) in mechanical engineering, in 2002, and the Ph.D. degree in bioengineering, in 2006. From 2016 to 2018, he was an Adjunct Professor of bioengineering with Politecnico di Torino, Italy. From 2019 to 2020, he was an Associate Professor with the University of Sassari, Italy. He is currently a Full Professor with Politecnico di Torino. He has co-authored more than 100 publications. He is the inventor of two patents. His research interests include high-resolution joint kinematics estimation, wearable sensors for locomotor capacity and performance assessment, and innovative approaches for neuro-muscular rehabilitation. He is a member of Italian National Group of Bioengineering. He is the President of Italian Society of Clinical Movement Analysis. He served on the Board of Directors of the 3-D Analysis of Human Movement Technical Group, ISB, from 2014 to 2018.

Open Access funding provided by 'Politecnico di Torino' within the CRUI CARE Agreement